HHS Public Access

Author manuscript

J Cancer Res Clin Oncol. Author manuscript; available in PMC 2017 July 01.

Published in final edited form as:

J Cancer Res Clin Oncol. 2016 July ; 142(7): 1475–1486. doi:10.1007/s00432-016-2165-9.

Rapid staining and imaging of subnuclear features to differentiate between malignant and benign breast tissues at a point-of-care setting

Jenna L. Mueller[1], **Jennifer E. Gallagher**[2], **Rhea Chitalia**[1], **Marlee Krieger**[1], **Alaattin Erkanli**[3], **Rebecca M. Willett**[4], **Joseph Geradts**[5], and **Nimmi Ramanujam**[1]

[1] Department of Biomedical Engineering, Duke University, 136 Hudson Hall Box 90281, Durham, NC 27708, USA

[2] Department of Surgery, Duke University Medical Center, 30 Medicine Drive White Zone, 3rd Floor, Suite 3570, Durham, NC 27710, USA

[3] Department of Biostatistics and Bioinformatics, Duke University, Brightleaf Square Suite 22B, 905 West Main Street, Durham, NC 27701, USA

[4] Department of Electrical and Computer Engineering, University of Wisconsin - Madison, 1415 Engineering Drive, Madison, WI 53706, USA

[5] Department of Pathology, Brigham and Women's Hospital, 75 Francis Street, Boston, MA 02115, USA

Abstract

Purpose—Histopathology is the clinical standard for tissue diagnosis; however, it requires tissue processing, laboratory personnel and infrastructure, and a highly trained pathologist to diagnose the tissue. Optical microscopy can provide real-time diagnosis, which could be used to inform the management of breast cancer. The goal of this work is to obtain images of tissue morphology through fluorescence microscopy and vital fluorescent stains and to develop a strategy to segment and quantify breast tissue features in order to enable automated tissue diagnosis.

Methods—We combined acriflavine staining, fluorescence microscopy, and a technique called sparse component analysis to segment nuclei and nucleoli, which are collectively referred to as acriflavine positive features (APFs). A series of variables, which included the density, area fraction, diameter, and spacing of APFs, were quantified from images taken from clinical core

Jenna L. Mueller, jenna.mueller@duke.edu.

Electronic supplementary material The online version of this article (doi:10.1007/s00432-016-2165-9) contains supplementary material, which is available to authorized users.

Compliance with ethical standards

Conflict of interest Dr. Ramanujam has founded a company called Zenalux Biomedical, and she and other team members have developed technologies related to this work where the investigators or Duke may benefit financially if this system is sold commercially. The other authors declare they have no conflict of interest.

Ethical approval All procedures performed in studies involving human participants were in accordance with the ethical standards of the institutional and/or national research committee and with the 1964 Helsinki Declaration and its later amendments or comparable ethical standards.

Informed consent Informed consent was obtained from all individual participants included in the study.

needle breast biopsies and used to create a multivariate classification model. The model was developed using a training data set and validated using an independent testing data set.

Results—The top performing classification model included the density and area fraction of smaller APFs (those less than 7 μm in diameter, which likely correspond to stained nucleoli).When applied to the independent testing set composed of 25 biopsy panels, the model achieved a sensitivity of 82 %, a specificity of 79 %, and an overall accuracy of 80 %.

Conclusions—These results indicate that our quantitative microscopy toolbox is a potentially viable approach for detecting the presence of malignancy in clinical core needle breast biopsies.

Keywords

Optical fluorescence imaging; Breast cancer; Image analysis; Logistic models

Background

Histopathology is the clinical standard for tissue diagnosis. Pathologists examine high-resolution images of small volumes of fixed, sectioned, and stained tissue (Kumar et al. 2005). When diagnosing cancer in particular, pathologists look for changes in tissue morphology including changes in nuclei and surrounding tissue. Nuclear changes that may indicate the presence of cancer include pleomorphism, increased nuclear-to-cytoplasmic ratio, increased nuclear density (hyperchromasia), decreased chromatin organization, and increased mitotic rate (Cohen 1996; Millot and Dufer 2000). Changes in the surrounding tissue include the presence of reactive stroma, which is composed of connective tissue, blood vessels, macrophages, lymphocytes, other inflammatory cells, and the presence of progressive infiltration, which involves the invasion and destruction of surrounding tissue (Cohen 1996; Millot and Dufer 2000). While histopathology is the gold standard, limitations include tissue processing, sectioning, and staining the tissue, which can take 30 min or more for frozen section diagnosis and more than 24 h for paraffin section diagnosis, and a highly trained pathologist to render a diagnostic evaluation.

Several clinical situations could benefit from more rapid and automated histologic processing, which could reduce the time and resources required between obtaining tissue and providing a diagnosis. For example, there is need for rapid detection of residual cancer on the surface of tumor resection specimens acquired during excisional surgeries, such as breast-conserving surgery (Jacobs 2008). Postoperative histopathologic assessment of the resected specimen is the current gold standard by which microscopic residual tumor in the margin is detected. Re-excision surgery is performed if residual cancer is found on the surface of the excised lumpectomy specimen, in order to reduce the risk of recurrence (Moran et al. 2014). Intra-operative frozen section analysis and touch prep cytology are used to assess surgical margins at the time of first surgery at a few select high-volume centers with dedicated resources and personnel. However, these techniques have not been widely adopted because they require laboratory personnel to be present during surgery including specially trained pathologists and sometimes radiologists. An additional clinical scenario that could benefit from more rapid histologic processing is the assessment of biopsy specimens at the point of care to confirm that a suspicious lesion is successfully sampled,

preventing an unnecessary repeat biopsy procedure. Rapid and low-cost histologic processing could also be potentially useful in settings lacking the resources necessary to perform standard histologic assessment (Adeyi 2011). For example, intermediate diagnostic biopsy is typically not performed between cancer screening and treatment in low- and middle-income countries (LMICs) due to the need for multiple visits (there is patient attrition with every clinic visit that is needed) and lack of resources (Rambau 2011). The number of pathologists in LMICs is small, even as a percentage of the total medical workforce. For example, there are only 15 pathologists in the entire country of Tanzania, which translates to 1 pathologist per 2.5 million people (Rambau 2011). Technologies that enable rapid, automated, low-cost histologic processing could address this unmet clinical need in LMICs.

In order to enable visualization of tissue at the point of care, many groups have developed microscopy techniques including reflectance and fluorescence microscopy (Balu et al. 2014; Drezek et al. 2003; Gareau et al. 2012; Muldoon et al. 2010; Schlichenmeyer et al. 2014), confocal microscopy (Clark et al. 2003; Dobbs et al. 2013; Karen et al. 2009; Tanbakuchi et al. 2009, 2010), and optical coherence tomography (OCT) (Boppart et al. 2004; Clark et al. 2004; Hsiung et al. 2007; Nguyen et al. 2009; Sun et al. 2013; Zysk et al. 2007) and demonstrated that morphological features can be detected with these approaches. While these techniques are well suited to enable real-time visualization of tissue morphology, quantitative image analysis is essential to enable objective interpretation and automated diagnosis. Toward this end, a few groups have combined automated nuclear morphometry and microscopy techniques to enable quantitative diagnosis during a procedure. For example, Nyirenda et al. (2011) applied nuclear morphometry to wide-field fluorescence microscopy images of a breast cancer rat model and found that area fraction, which is the nuclear area divided by the total area, achieved 97 % sensitivity and 97 % specificity for tumor detection. Previously, our group employed a topically applied fluores-cent contrast agent called acriflavine and a high-resolution fluorescence microendoscope to visualize the microanatomical features in resected preclinical tumor sarcoma margins (Mueller et al. 2013). In this study, we developed a technique for segmenting acriflavine positive features (APFs) from the heterogeneous preclinical sarcoma margins using an algorithm called sparse component analysis (SCA) (Mueller et al. 2013), which has been used in the image processing community for image compression. While APFs roughly correspond to nuclei, in some cases nucleic acids are concentrated within the nucleoli of neoplastic cells; therefore, we refer to these acriflavine positive features as APFs throughout this work. SCA accurately segmented APFs from images that contained tumor, muscle, and adi-pose tissue types, and differences in APF density were used to diagnose positive tumor margins (Mueller et al. 2013).

The goal of this study was to test the robustness of our quantitative microscopy toolbox to detect the presence of malignancy in clinical core needle breast biopsies, and to assess whether this approach can be extended from a pre-clinical sarcoma model to clinical specimens for point-of-care procedures associated with breast cancer diagnosis. A model was optimized with a training data set of 26 biopsy panels and then was prospectively applied to a testing data set of 25 biopsy panels to assess whether our approach could be

used to accurately diagnose clinical breast biopsy specimens into their specific histopathologic diagnoses.

Methods

Patient population

This study was performed under a protocol approved by the Duke University Institutional Review Board (Protocol Number: Pro00008003). Eighty patients age 18 and over undergoing core needle breast biopsy procedures at Duke University Medical Center gave written consent before enrolling into the study. In addition to imaging tissue, characteristics were tabulated for each patient including age, body mass index, receptor status, menopausal status, and mammographic breast density. For mammographic breast density, each patient was assigned a value based on their pre-surgery mammogram: 1 (fatty), 2 (scattered fibroglandular), 3 (heterogeneously dense), or 4 (extremely dense). This demographic information is included in Table 1.

Imaging system and contrast agent

A high-resolution fluorescence microendoscope that has been described previously (Muldoon et al. 2007) was used to capture images of breast tissue. Briefly, the microendoscope contained a 455-nm light emitting diode, excitation filter, dichroic mirror, 10× objective, emission filter, and CCD camera. The light was directed to the sample through a flexible fiber bundle composed of 30,000 fibers that yielded a circular field of view of approximately 750 μm in diameter. The resolution of the system was approximately 4.4 μm as determined by Muldoon et al. (2007). Acriflavine was selected as a topical contrast agent because it highlights tissue morphology seconds after being applied. Specifically, acriflavine reversibly associates with RNA and DNA and has also been shown to stain collagen and muscle fibers (Ferguson and Denny 1991; Krolenko et al. 2006). Acriflavine was dissolved in phosphate-buffered saline solution (0.01 % w/v, Sigma-Aldrich) and was topically applied to excised breast tissue immediately prior to imaging with the microendoscope.

Imaging protocol

During core needle breast biopsy procedures, several biopsies were taken from the suspicious area. Our research team was usually handed the first biopsy, which typically came from the center of the suspicious lesion. This was not a research biopsy collected for our particular study; rather, our research team intercepted the first biopsy collected before it was sent to the pathology laboratory. After the biopsy was acquired (typically within 10 min of the procedure being performed), acriflavine was applied to the surface of the specimen. After 30 s, the distal end of the fiber bundle was placed in contact with the tissue and images were acquired. The biopsy was scanned lengthwise by systematically moving the probe in 1 mm increments over the tissue surface. Once one side was scanned, the biopsy was rotated 180° and the lengthwise scanning process was repeated. In order to improve the accuracy and reproducibility of these movements, the fiber bundle was secured in a custom probe holder, which was mounted on an *x*–*y* translation stage. Biopsies ranged from 10 to 20 mm in length and imaging took approximately 10–15 min to complete.

After imaging was completed, the surface of the specimen was inked for pathological co-registration. In order to maintain the proper orientation for pathological evaluation, each half of the biopsy specimen was inked with a different color (see Fig. 1). After imaging and inking were complete, the tissue was returned for standard of care pathologic processing. Specifically, pathology sections were cut longitudinally to provide a cross section of the entire length of the biopsy specimen. As per standard clinical laboratory protocol, our study breast pathologist (J.G), who was blinded to the results of fluorescence microscopic imaging, reviewed hematoxylin and eosin (H&E) sections from 3 levels from each diagnostic paraffin block. A diagnosis was acquired for the ends of each biopsy (the last 1 mm) as well as for the middle portion of each biopsy (the central 8–18 mm). For malignant biopsies, the biopsy diagnosis was based on the highest grade of malignancy within the middle section. For benign biopsies, the biopsy diagnosis is based on the average tissue composition within the middle section. Biopsy panels consisted of the images in the central 8–18 mm and did not include the ends (the last 1 mm) because the ends of the biopsies were often extremely thin and difficult to get in focus. Since images were acquired every 1 mm and the biopsy was imaged twice, between 16 and 36 images were acquired of the middle portion of each biopsy specimen.

Biopsy analysis

A total of 80 patients were recruited for this study. However, 5 patients were used for a feasibility study prior to 2011. Eight patients were counted as screen fails because they became ineligible after consenting to the study. An additional 8 patients were excluded from the study due to various logistical issues that were unrelated to the actual implementation of our protocol. In total our study team was able to successfully image 59 biopsy specimens with a corresponding pathologic diagnosis, 5 of which were stereotactic core biopsies and 54 of which were ultrasound-guided core needle biopsies. For our analysis, the 5 stereotactic biopsies were removed from the data set because the samples were extremely fatty. The 2 biopsies from the other benign category (which included a lymph node and hematoma) and the 1 ductal carcinoma in situ (DCIS) biopsy were removed since only one sample was acquired of each of these pathologies, and no conclusions could be drawn. This decreased the total number of biopsies panels from 54 to 51. This information is summarized in Fig. 2.

Acriflavine positive features (APFs) were segmented through application of a technique called sparse component analysis (SCA), which has been described previously (Mueller et al. 2013). All image processing and analysis were completed in MATLAB (2013b, Mathworks Inc., Natick, MA). First, images were cropped in order to discard the rim of the fiber bundle. Additionally, a low-pass Gaussian filter was applied to remove the fiber core pattern that was superimposed onto the images. Next, SCA was used to separate APFs from fibrous and adipose structures in heterogeneous images. After SCA was applied to isolate APFs, the circle transform (CT) was applied to compute the size and density of APFs. CT was chosen to quantify diagnostic variables associated with APFs because it detects approximately circular objects (i.e., APFs), can distinguish overlapping circular APFs, and is easy to tune (Ballard 1981).

Next, the variables were calculated from segmented images. Variables were designed to capture disease features typically seen in H&E-stained slides, such as increased nuclear density or nuclear pleomorphism (the variation in size and shape of nuclei) (Cohen 1996; Millot and Dufer 2000). Specifically, variables include density of APFs (the number of APFs in a unit area), area fraction (the total APF area divided by the total area), minimum internuclear distance (the distance between the center of an APF and the center of the next closest or nearest neighboring APF), and diameter (the output given by CT). Density and area fraction represent scalar variables in which only one value is returned for each image. Conversely, the minimum internuclear distance and diameter represent vector variables in which a value is calculated for each APF within the image. In order to consolidate the vector variables into a single value, the mean IND and mean diameter were calculated for each image.

In order to develop a classification model, the biopsies were divided into a testing set and training set (Table 2). Different combinations of the variables described above were investigated through the use of the training data set to evaluate performance of the multivariate model, which was based on logistic regression in the SAS programming environment. For each biopsy, the logistic regression model yields a probability value that the biopsy is malignant. Probabilities values can vary from 0 to 1 with 1 corresponding to a 100 % probability that the biopsy is malignant. Receiver operator characteristic (ROC) curves were constructed with the probability values for the biopsies in the training data set using a web-based tool (Youden 1950). The area under the curve (AUC) associated with each ROC curve was tabulated. Then the best performing models (with the highest AUCs) were applied to the testing data set, and the probability values were used to construct ROC curves. The model that yielded the highest AUC for the testing data set was selected and used to examine which biopsies were correctly and incorrectly classified. A cut point on the ROC curve was selected based on the quantity $F = (1\text{-sensitivity})^2 + (1\text{-specificity})^2$, which is minimized at the optimal sensitivity and specificity.

Results

Demographic information

The breakdown of the 54 ultrasound-guided biopsies specimens imaged in this study is shown in Table 1. Of the 54 biopsies, 23 were malignant and 31 were benign specimens. The 23 malignant cases were comprised of 20 invasive ductal carcinomas (IDC), 2 invasive lobular carcinomas (ILC), and 1 ductal carcinoma in situ (DCIS). Of the 31 benign biopsies, 2 contained primarily adipose or fibroadipose tissue, 21 contained primarily fibroglandular, fibrous, or glandular tissue, 6 were either fibroadenomas or papillomas and 2 contained other benign pathologies including a lymph node and a hematoma. The 1 lymph node, 1 hematoma, and 1 DCIS biopsy were excluded from further analysis since only one sample was acquired of each of these pathologies, and no conclusions could be drawn.

Biopsy analysis

Figure 3 shows a representative example of a malignant and benign biopsy from our study. Each side of the biopsy was scanned lengthwise—the left column corresponds to side 1 and

the right column corresponds to side 2. A summary diagnosis is given for the middle portion each biopsy (the central 8–18 mm). The malignant example in Fig. 3a contains IDC and fibrous tissue, and the benign example in Fig. 3b contains fibroglandular and adipose tissue. For visualization purposes, APFs that were larger than 7 μm in diameter were false colored red, and APFs that were less than or equal to 7 μm in diameter were false colored green and overlaid onto the original image (column 3). The threshold of '7 μm' was chosen because APFs smaller than the threshold are likely to correspond to nucleoli, while APFs larger than the threshold are likely to correspond to nuclei (Nandakumar et al. 2012). Specifically, others have found that nuclear volume of human breast cancer cell lines ranged from approximately 200–1500 μm^3 while nucleolar volume ranges from 5 to 170 μm^3 (Nandakumar et al. 2012). If the assumption is made that nuclei and nucleoli are approximately spherical, this corresponds 7–14 μm in diameter for nuclei and 2–7 μm in diameter for nucleoli, suggesting that threshold of '7 μm' may lead to some separation between nuclei and nucleoli. To confirm this range of sizes, we manually circled nuclei and nucleoli in H&E images of various breast pathologies. Results in Fig. 4 indicate that the diameter of most nucleoli is less than or equal to 7 μm while most nuclei are greater than 7 μm in diameter; thus, 7 μm appears to be an appropriate threshold to separate nuclei from nucleoli.

Table 2 shows how many biopsies fell into each pathological category for the biopsy analysis. Specifically, the biopsies from each pathologic category were randomly divided into a training set and testing set in order to develop and assess various diagnostic models. For example, the 20 IDC biopsies were randomly divided between the training and testing sets such that each set contained 10 IDC biopsies. The training and testing sets contained 26 and 25 biopsies, respectively.

Figure 5a–c shows boxplots of the average density, area fraction, internuclear distance, and diameter calculated from the malignant ($n = 11$) and benign ($n = 15$) biopsies in the training set. Average density, area fraction, internuclear distance, and diameter were calculated for all APFs, smaller APFs (green), and larger APFs (red). As expected, each density and area fraction boxplot reflected higher concentrations of APFs for the malignant compared to the benign tissue types. The density of the smaller APFs (green) yielded the most significant difference between malignant and benign biopsies ($p = 0.0095$). Similarly, area fraction of the smaller APFs (green) led to the most significant differences between malignant and benign biopsies. The average diameter of all APFs also led to a significant difference between malignant and benign biopsies ($p = 0.022$). Thus, the top performing variables, which included the density of the smaller APFs (green), the area fraction of the smaller APFs (green), and the average diameter of all APFs, were used to create various univariate and multivariate models.

For each univariate and multivariate model, the AUCs achieved with the training and testing sets were tabulated and are shown in Fig. 6a. The density of the smaller APFs (green) combined with the area fraction of the smaller APFs (green) achieved the highest average AUC of 0.83. No additional improvement in performance was gained by using three variables. The ROC curve for this top performing model is shown for both the training and testing data sets in Fig. 6b. The optimal cut point on the testing set curve in Fig. 6a was used

to determine the performance metrics listed in Fig. 6c. Specifically, the model yielded a sensitivity of 82 %, specificity of 79 %, and overall accuracy of 80 %. In total, there were 9 true positives, 2 false negatives, 11 true negatives, and 3 false positives. False positive biopsies included 1 fibroadipose and 2 fibrous biopsies, while both false negative biopsies contained IDC embedded in a fibrous background. Of the 2 false positive biopsies, 2 contained notable amounts inflammation and the other contained notable amounts of fat necrosis. A representative false negative and false positive biopsy is shown in Supplementary Figure 1.

Discussion

In this study, we demonstrate that fluorescent microscopy of acriflavine-stained tissue combined with an algorithm that leverages SCA + CT provide a rapid, non-destructive, and automated strategy for quantitative pathology of heterogeneous, fresh, core needle biopsies. The primary source of contrast in this study was the density and area fraction of the smaller APFs. Specifically, the density of smaller APFs (green) + area fraction of the smaller APFs (green) achieved the highest average AUC of 0.83. As expected, there were significantly higher density and area fraction for malignant biopsies (Fig. 5). This trend was also seen in our previous work in which the density of the smaller features led to more significant differences between positive and negative images of excised preclinical sarcoma margins (Mueller et al. 2013). The density of the smaller APFs likely provides more contrast between malignant and benign images because nucleic acids are highly concentrated within the nucleoli of malignant cells while they are more diffuse within benign cells. For example, the presence of prominent or multiple nucleoli is associated with a high nuclear grade, which has been shown to correlate with the aggressive potential of breast carcinomas (Rakha et al. 2010). Thus, malignant regions or images are likely to contain a larger amount of the smaller APFs.

A significant strength of this approach is no additional tuning or optimization of SCA + CT is required when transitioning the application from preclinical sarcoma margins to clinical core needle breast biopsies. Thus, this work demonstrates that this methodology can be easily applied to a variety of different organ sites where point-of-care quantitative pathology would be useful. Specifically, this approach could be used to evaluate the adequacy of core needle biopsies immediately after the tissue is acquired and provide a preliminary diagnosis at the point of care. Additionally, we observed that acriflavine staining does not interfere with H&E processing or visualization. Thus, the system is non-destructive and is compatible with downstream histology and molecular analysis. Another strength of this study is that we were able to image the first core biopsy, which typically came from the center of the suspicious mass in the patient. Ultimately this allowed us to acquire a high yield of malignant images in our data set. Additionally, our study did not require removing additional tissue from the patient (as would be the case if our study required taking a separate research biopsy).

However, since we merely intercepted the tissue between the biopsy procedure and the pathology laboratory, the tissue that we imaged and inked had to be placed in formalin with the other biopsies (in order to follow standard biopsy pathology protocols). Often this

resulted in fragmentation of the tissue, which prevented our research team from acquiring a three-prong pathology diagnosis. For example, if the ends of a biopsy broke off in the vial with the other biopsies, then we did not acquire a diagnosis for the ends of the biopsy (rather we only acquired a diagnosis for the middle portion of the biopsy). Additionally, we found that it was difficult to acquire high-quality images of the ends of the biopsies with our device because the tissue was extremely thin and difficult to get in focus. Consequently, we could not use many of the images at the end of the biopsies and therefore removed them from the biopsy panels prior to image analysis.

Misclassified biopsies included 1 fibroadipose biopsy, 2 fibrous biopsies, and 2 IDC biopsies that were embedded in a fibrous background. Two of the 3 false positive biopsies included fibrous biopsies with notable amounts of inflammation, which can be highly cellular and difficult to distinguish from malignant tissue types. The other false positive biopsy contained large amounts of fat necrosis, which stained brightly with acriflavine and appeared highly cellular with the high-resolution microendoscope. Conversely, both false negative biopsies contained IDC embedded in a fibrous background, which yielded hazy images and likely prevented detection of APFs. While each biopsy panel was categorized as IDC, ILC etc., based on their primary diagnosis, other tissue types are often present. Additionally, there may be differing amounts of IDC or ILC, which was not quantified in the pathological diagnosis. To better assess how heterogeneity or partial volume errors affect our diagnostic model, future studies could employ alternative pathologic strategies that enable us to quantify the relative amounts of malignant versus benign tissue or fibrous versus adipose tissue within a biopsy specimen. Additionally, the sample size included in this study is small; thus, future studies could apply the diagnostic model developed here to a much larger data set for further validation.

One shortcoming from the work shown here is that the fluorescence microendoscope collects light from several cell layers, which contributes to background fluorescence or blur coming from deeper layers in the sample (Muldoon et al. 2007). This can lead to hazy images, which can affect the ability of algorithms to accurately segment APFs (Mueller et al. 2013). Background fluorescence could be reduced through leveraging optical sectioning techniques, such as confocal microscopy or structured illumination microscopy (see Supplementary Figure 2).While confocal microscopy can achieve high spatial resolution (<1 μm), the need for beam scanning limits the volume of tissue that can be surveyed in a given amount of time and ultimately limits it translatability to the clinical practice. Structured illumination microscopy has been shown to perform comparably to confocal microscopy with respect to optical sectioning and signal-to-noise ratio, particularly in superficial tissues (Chasles et al. 2007; Gustafsson 2000; Hagen et al. 2012). However, structured illumination microscopy has the added advantage of full-field illumination and non-des-canned detection, thus lowering the complexity compared to confocal scanning systems and increasing the speed with which microscopy of large tissue areas can be performed. Thus, structured illumination microscopy in combination with appropriate segmentation algorithms could be leveraged to image large areas of tissue at high resolution and provide quantitative information in a clinically relevant time window.

Conclusions

In conclusion, acriflavine staining and fluorescence microscopy combined with SCA + CT can be used to quantitatively diagnose breast disease. Together, this work yields an optimized set of tools that are capable of imaging tissue at high resolution with no tissue processing and that can automatically segment and quantify those specimens. Ultimately, this platform provides a potentially useful adjunct to histopathology techniques by providing quality control at the point-of-care setting.

Supplementary Material

Refer to Web version on PubMed Central for supplementary material.

Acknowledgments

We thank Dr. Rebecca Richards-Kortum and her student, Jessica Dobbs, for providing the imaging system and guidance on image acquisition. We acknowledge financial support from Department of Defense Grant Number W81XWH-09-1-0410 and NIH Grant Number 1R01EB01157.

Funding This study was funded by the Department of Defense (Grant Number W81XWH-09-1-0410) and the NIH (Grant Number 1R01EB01157).

References

Adeyi OA. Pathology services in developing countries-The West African experience. Arch Pathol Lab Med. 2011; 135:183–186. [PubMed: 21284434]

Ballard D. Generalizing the hough transform to detect arbitrary shapes, vol 13. Pattern Recognition. 1981

Balu M, et al. Distinguishing between benign and malignant melanocytic nevi by in vivo multiphoton microscopy. Cancer Res. 2014; 74:2688–2697. doi:10.1158/0008-5472.CAN-13-2582. [PubMed: 24686168]

Boppart SA, Luo W, Marks DL, Singletary KW. Optical coherence tomography: feasibility for basic research and image-guided surgery of breast cancer. Breast Cancer Res Treat. 2004; 84:85–97. doi: 10.1023/B:BREA.0000018401.13609.54. [PubMed: 14999139]

Chasles F, Dubertret B, Boccara AC. Optimization and characterization of a structured illumination microscope. Opt Express. 2007; 15:16130–16140. [PubMed: 19550902]

Clark AL, Gillenwater AM, Collier TG, Alizadeh-Naderi R, El-Naggar AK, Richards-Kortum RR. Confocal microscopy for real-time detection of oral cavity neoplasia. Clin Cancer Res. 2003; 9:4714–4721. [PubMed: 14581341]

Clark AL, Gillenwater A, Alizadeh-Naderi R, El-Naggar AK, Richards-Kortum R. Detection and diagnosis of oral neoplasia with an optical coherence microscope. J Biomed Opt. 2004; 9:1271–1280. doi:10.1117/1.1805558. [PubMed: 15568948]

Cohen C. Image cytometric analysis in pathology. Hum Pathol. 1996; 27:482–493. [PubMed: 8621187]

Dobbs JL, Ding H, Benveniste AP, Kuerer HM, Krishnamurthy S, Yang W, Richards-Kortum R. Feasibility of confocal fluorescence microscopy for real-time evaluation of neoplasia in fresh human breast tissue. J Biomed Opt. 2013; 18:106016. doi:10.1117/1.JBO.18.10.106016. [PubMed: 24165742]

Drezek RA, et al. Optical imaging of the cervix. Cancer. 2003; 98:2015–2027. doi:10.1002/cncr.11678. [PubMed: 14603538]

Ferguson LR, Denny WA. The genetic toxicology of acridines. Mutat Res. 1991; 258:123–160. [PubMed: 1881402]

Gareau DS, Jeon H, Nehal KS, Rajadhyaksha M. Rapid screening of cancer margins in tissue with multimodal confocal microscopy. J Surg Res. 2012; 178:533–538. doi:10.1016/j.jss.2012.05.059. [PubMed: 22721570]

Gustafsson MGL. Surpassing the lateral resolution limit by a factor of two using structured illumination microscopy. J Microsc Oxford. 2000; 198:82–87. doi:10.1046/j.1365-2818.2000.00710.x. [PubMed: 10810003]

Hagen N, Gao L, Tkaczyk TS. Quantitative sectioning and noise analysis for structured illumination microscopy. Opt Express. 2012; 20:403–413. doi:10.1364/OE.20.000403. [PubMed: 22274364]

Hsiung PL, Phatak DR, Chen Y, Aguirre AD, Fujimoto JG, Connolly JL. Benign and malignant lesions in the human breast depicted with ultrahigh resolution and three-dimensional optical coherence tomography. Radiology. 2007; 244:865–874. doi:10.1148/radiol.2443061536. [PubMed: 17630358]

Jacobs L. Positive margins: the challenge continues for breast surgeons. Ann Surg Oncol. 2008; 15:1271–1272. doi:10.1245/s10434-007-9766-0. [PubMed: 18320287]

Karen JK, Gareau DS, Dusza SW, Tudisco M, Rajadhyaksha M, Nehal KS. Detection of basal cell carcinomas in Mohs excisions with fluorescence confocal mosaicing microscopy. Br J Dermatol. 2009; 160:1242–1250. doi:10.1111/j.1365-2133.2009.09141.x. [PubMed: 19416248]

Krolenko SA, Adamyan SY, Belyaeva TN, Mozhenok TP. Acridine orange accumulation in acid organelles of normal and vacuolated frog skeletal muscle fibres. Cell Biol Int. 2006; 30:933–939. doi:10.1016/j.cellbi.2006.06.017. [PubMed: 16895760]

Kumar, V.; Abbas, A.; Fausto, N. Robbins and Cotran pathologic basis of disease. 7th edn.. Elsevier Saunders; Philadelphia: 2005.

Millot C, Dufer J. Clinical applications of image cytometry to human tumour analysis. Histol Histopathol. 2000; 15:1185–1200. [PubMed: 11005244]

Moran MS, et al. Society of surgical oncology-American Society for radiation oncology consensus guideline on margins for breast-conserving surgery with whole-breast irradiation in stages I and II invasive breast cancer. J Clin Oncol. 2014; 32:1507–1516. [PubMed: 24516019]

Mueller JL, et al. Quantitative segmentation of fluorescence microscopy images of heterogeneous tissue: application to the detection of residual disease in tumor margins. PLoS ONE. 2013; 8:e66198. doi:10.1371/journal.pone.0066198. [PubMed: 23824589]

Muldoon TJ, Pierce MC, Nida DL, Williams MD, Gillenwater A, Richards-Kortum R. Subcellular-resolution molecular imaging within living tissue by fiber microendoscopy. Opt Express. 2007; 15:16413–16423. [PubMed: 19550931]

Muldoon TJ, et al. Evaluation of quantitative image analysis criteria for the high-resolution microendoscopic detection of neoplasia in Barrett's esophagus. J Biomed Opt. 2010; 15:026027. doi:10.1117/1.3406386. [PubMed: 20459272]

Nandakumar V, et al. Isotropic 3D nuclear morphometry of normal, fibrocystic and malignant breast epithelial cells reveals new structural alterations. PLoS ONE. 2012; 7:e29230. doi:10.1371/journal.pone.0029230. [PubMed: 22242161]

Nguyen FT, et al. Intraoperative evaluation of breast tumor margins with optical coherence tomography. Cancer Res. 2009; 69:8790–8796. doi:10.1158/0008-5472.CAN-08-4340. [PubMed: 19910294]

Nyirenda N, Farkas DL, Ramanujan VK. Preclinical evaluation of nuclear morphometry and tissue topology for breast carcinoma detection and margin assessment. Breast Cancer Res Treat. 2011; 126:345–354. doi:10.1007/s10549-010-0914-z. [PubMed: 20446030]

Rakha EA, et al. Breast cancer prognostic classification in the molecular era: the role of histological grade. Breast Cancer Res. 2010; 12:1–12.

Rambau PF. Pathology practice in a resource-poor setting: Mwanza, Tanzania. Arch Pathol Lab Med. 2011; 135:191–193. doi:10.1043/1543-2165-135.2.191. [PubMed: 21284436]

Schlichenmeyer TC, Wang M, Elfer KN, Brown JQ. Video-rate structured illumination microscopy for high-throughput imaging of large tissue areas Biomed. Opt Express. 2014; 5:366–377. doi:10.1364/BOE.5.000366.

Sun JG, Adie SG, Chaney EJ, Boppart SA. Segmentation and correlation of optical coherence tomography and X-ray images for breast cancer diagnostics. J Innov Opt Health Sci. 2013; 6:1350015. doi:10.1142/S1793545813500156. [PubMed: 24533035]

Tanbakuchi AA, Rouse AR, Udovich JA, Hatch KD, Gmitro AF. Clinical confocal microlaparoscope for real-time in vivo optical biopsies. J Biomed Opt. 2009; 14:044030. doi:10.1117/1.3207139. [PubMed: 19725741]

Tanbakuchi AA, Udovich JA, Rouse AR, Hatch KD, Gmitro AF. In vivo imaging of ovarian tissue using a novel confocal microlaparoscope. Am J Obstet Gynecol. 2010; 202:90.e91–90.e99. doi: 10.1016/j.ajog.2009.07.027. [PubMed: 19800605]

Youden WJ. Index for rating diagnostic tests. Cancer. 1950; 3:32–35. [PubMed: 15405679]

Zysk AM, Nguyen FT, Oldenburg AL, Marks DL, Boppart SA. Optical coherence tomography: a review of clinical development from bench to bedside. J Biomed Opt. 2007; 12:051403. doi: 10.1117/1.2793736. [PubMed: 17994864]

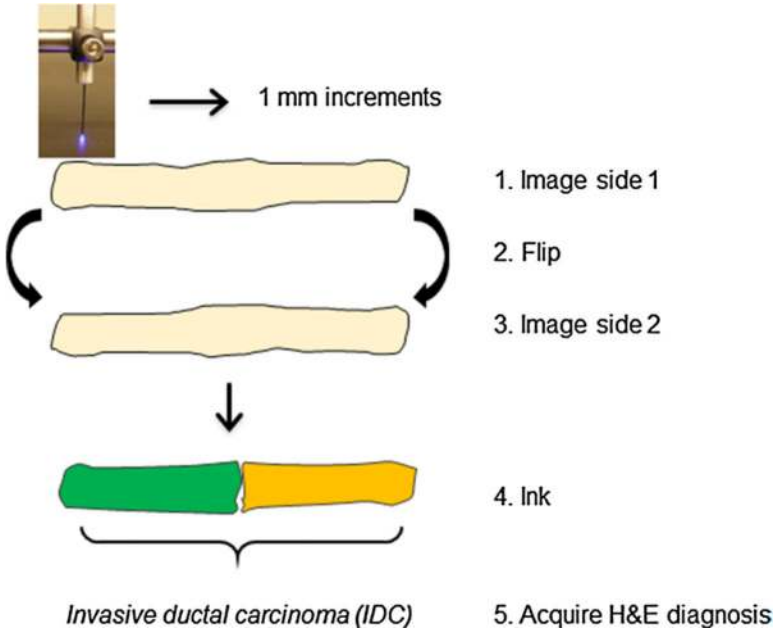

Fig. 1.

Illustration of imaging and inking protocol. First acriflavine was topically applied to the biopsy, and side 1 was imaged by moving the probe in 1-mm increments along the length of the biopsy. Then the biopsy was flipped 180°, and side 2 was imaged in 1-mm increments. Next the biopsy was inked with two colors to maintain orientation—for example, *green ink* was applied on the left side, and *orange ink* was applied on the right side. Then the biopsy was submitted for H&E processing and an aggregate diagnosis was given for the middle component (the center 8–18 mm)

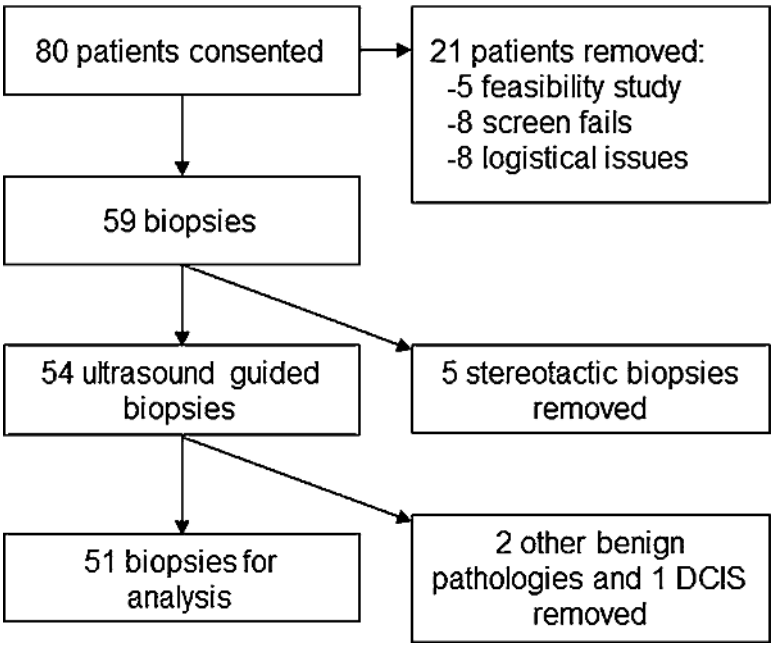

Fig. 2.
Inclusion criteria for the biopsy data set

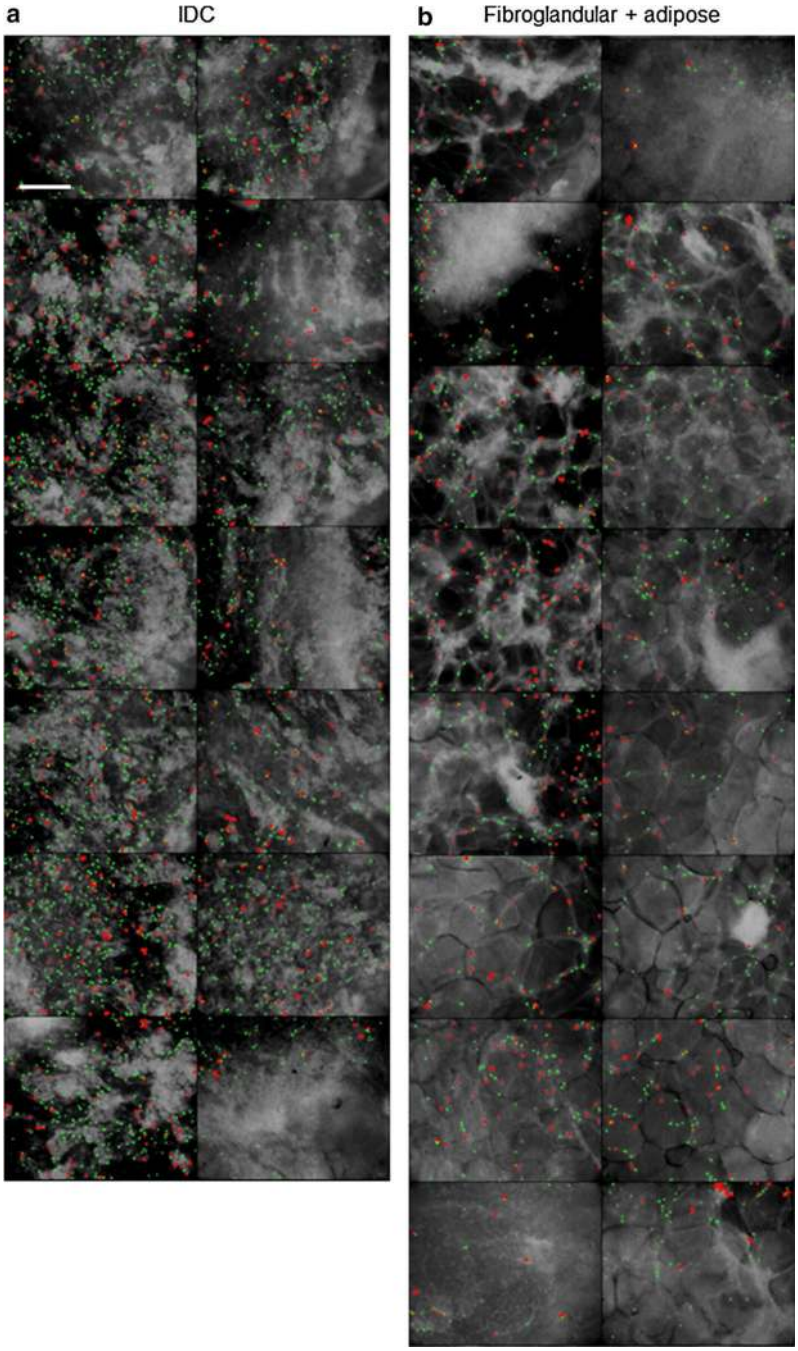

Fig. 3.

Application of sparse component analysis (SCA) and circle transform (CT) to representative biopsy panels. A representative positive and negative breast biopsy panels are shown in **a**, **b**, respectively. Each side of the biopsy was scanned lengthwise—side 1 corresponds to the left column and side 2 corresponds to the right column. Images are shown as an overlay in which the smaller acriflavine positive features (APFs) (<7 μm diameter) are false colored green. The background was dimmed to enhance visualization in the overlay. *Scale bar* is 200 μm

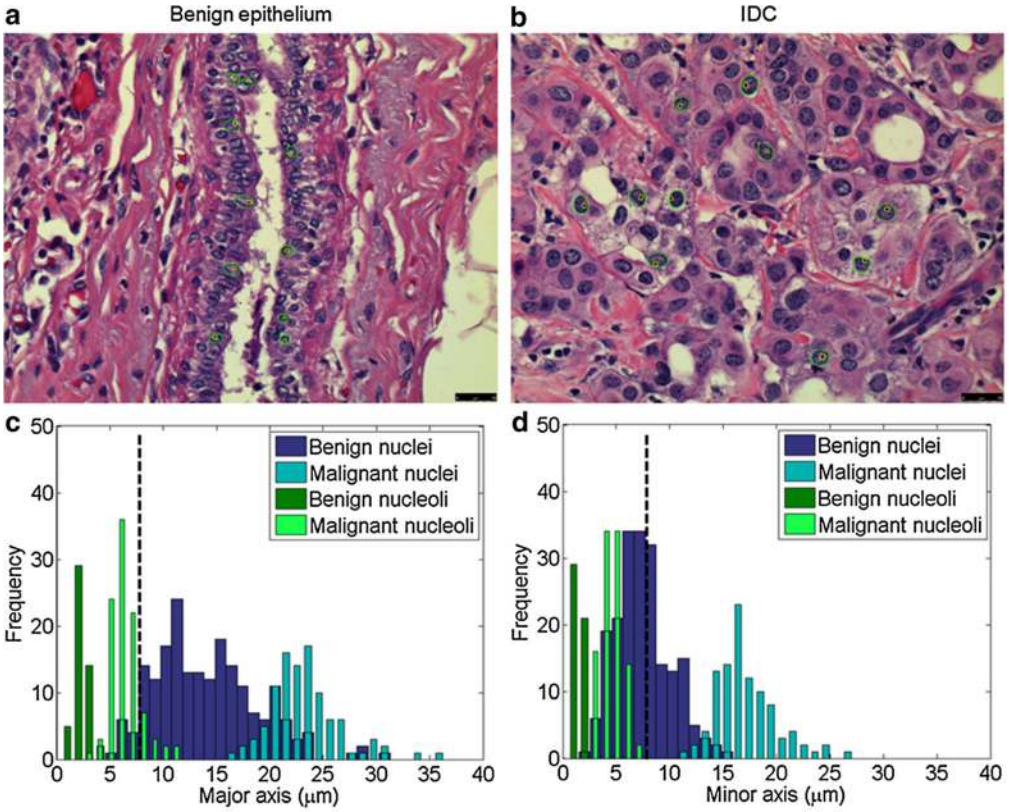

e

Feature	Major axis (μm, avg ± std)	Minor axis (μm, avg ± std)
Nuclei		
IDC	24.2 ± 3.8	17.2 ± 2.8
ILC	23.5 ± 2.7	17.9 ± 2.6
Benign epithelium	16.6 ± 3.7	10.4 ± 2.5
Stromal cells	17.2 ± 5.0	6.1 ± 1.8
Adipocytes	15.2 ± 4.0	7.8 ± 2.1
Lymphocytes	9.6 ± 1.8	7.8 ± 1.5
Nucleoli		
IDC	6.7 ± 1.0	5.1 ± 0.9
ILC	7.3 ± 1.7	5.2 ± 1.0
Benign epithelium	2.8 ± 0.6	2.0 ± 0.4

Fig. 4.

Representative H&E-stained sections of benign epithelium and invasive ductal carcinoma (IDC) are shown in **a**, **b**. In each image, nuclei and nucleoli are outlined in *green* and *yellow*, respectively. *Scale bar* 25 μm. Histograms showing the frequency distribution of the major axis and minor axis of malignant and benign nuclei and nucleoli can be seen in **c**, **d,** respectively. The *black dotted line* indicates the threshold of 7 μm. The average major and minor axis of the nuclei or nucleoli circled in a set of images are reported in **e** ($n = 50$ for each row)

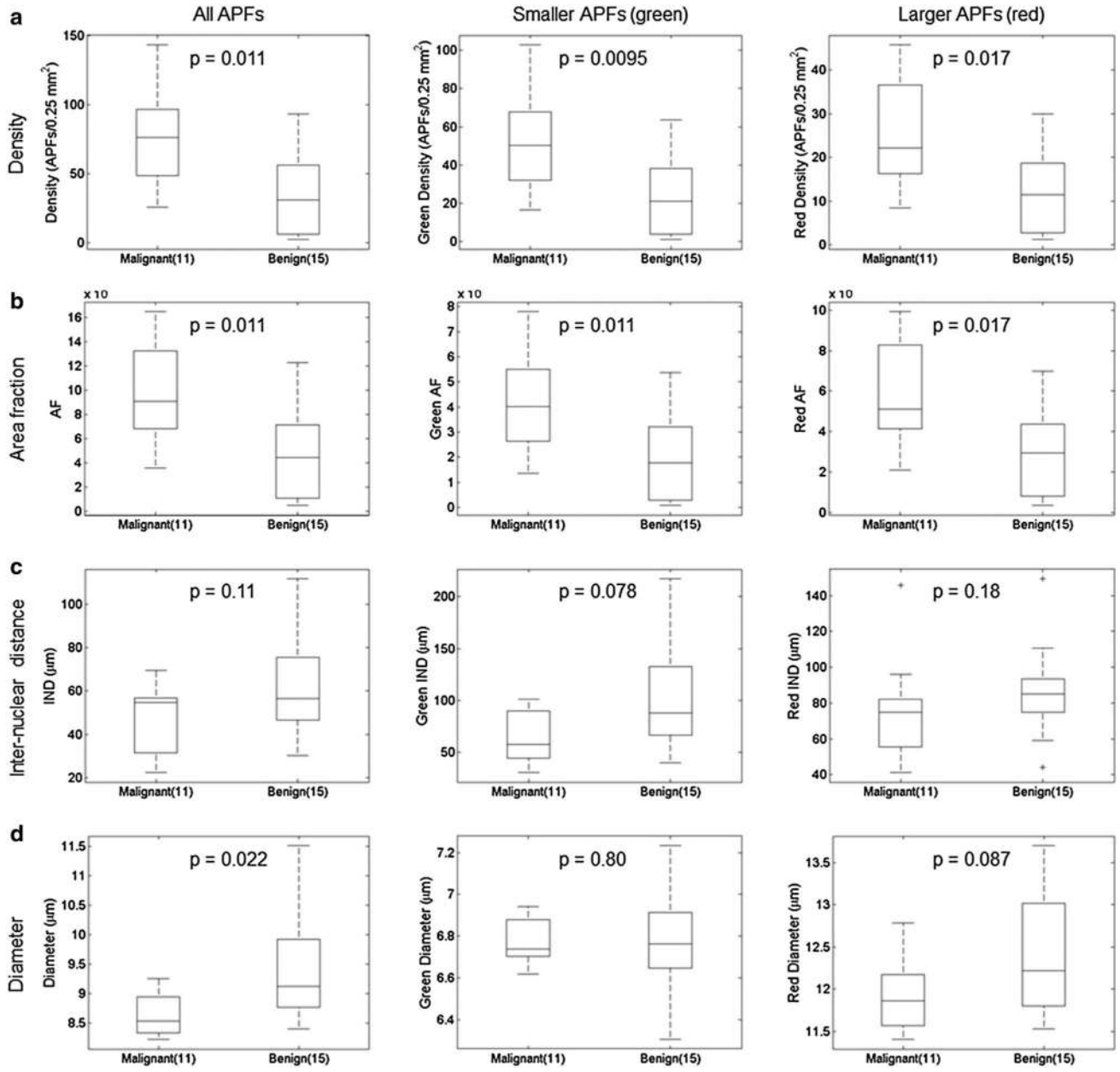

Fig. 5.

Variables calculated for the training data set. Variables were calculated from 11 malignant and 15 benign biopsies. *Boxplots* were created for the density, area fraction, average internuclear distance, and average diameter and are shown in **a–d,** respectively. Calcula tions were completed for all APFs, smaller APFs (green), and larger APFs (red) and are shown in columns 1–3, respectively. *p* values calculated from Wilcoxon rank sums are shown in each *boxplot.* All *p* values less than 0.05 are considered significant

a

Variable(s) included in model	Training AUC (n = 26)	Testing AUC (n = 25)	Average AUC
Density of smaller APFs (green)	0.81	0.79	0.80
Area fraction of smaller APFs (green)	0.80	0.81	0.80
Diameter of all APFs	0.77	0.76	0.76
Density of smaller APFs (green) + Area fraction of smaller APFs (green)	0.86	0.80	0.83
Density of smaller APFs (green) + Diameter of all APFs	0.81	0.81	0.81
Area fraction of smaller APFs (green) + Diameter of all APFs	0.79	0.82	0.81
Density of smaller APFs (green) + Area fraction of smaller APFs (green) + Diameter of all APFs	0.84	0.75	0.80

b

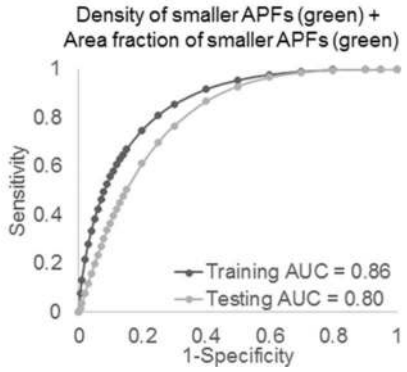

c

Metric	Performance
Sensitivity	82%
Specificity	79%
Positive predictive value	75%
Negative predictive value	85%
Accuracy	80%

Fig. 6.

Top performing variables from Fig. 5 were used to create different univariate and multivariate models. Models were developed based on the training data set and applied to the testing data set. The AUCs achieved with the training and testing sets, as well as the average AUC, are shown in **a**. A ROC curve of the top performing model is shown in **b**. The ROC plot contains the ROC curve associated with the training and testing data sets. The area under the curve for the training data set (training AUC) and testing data set (testing AUC) is shown on the plot. The performance metrics associated with the optimal cut point on the testing data set ROC curve are shown in **c**. Metrics include sensitivity, specificity, positive predictive value, negative predictive value, and overall accuracy

Table 1

Patient demographics

Characteristic	Biopsies
Ultrasound-guided biopsies	54
Primary histology	54
Malignant and premalignant	23 (42.6 %)
Invasive ductal carcinoma (IDC)	20 (37.0 %)
Invasive lobular carcinoma (ILC)	2 (3.7 %)
Ductal carcinoma in situ (DCIS)	1 (1.9 %)
Benign	31 (57.4 %)
Adipose, fibroadipose	2 (3.7 %)
Fibroglandular, fibrous, glandular	21 (38.9 %)
Fibroadenoma, papilloma	6 (11.1 %)
Other (lymph node, hematoma)	2 (3.7 %)
Avg. age (range)	53.1 (19–85)
Avg. BMI (range)	31.5 (17.6–61.7)
Tumor receptor status (invasive only)	
ER +, –	16 (72.7 %), 6 (27.3 %)
PR +, –	15 (68.2 %), 7 (31.8 %)
HER-2/neu +/–	2 (9.1 %), 20 (90.9 %)
Triple negative	5 (22.7 %)
Menopausal status	
Pre	19 (35.2 %)
Peri	1 (1.9 %)
Post	34 (63.0 %)
Breast density[a]	
1	1 (2.1 %)
2	18 (37.5 %)
3	24 (50.0 %)
4	5 (10.4 %)

[a]Breast density was acquired for 48 out of 54 patients since 6 mammograms were taken at other institutions

Table 2

Biopsies included in analysis

Primary histology	Total biopsies	Training set	Testing set
Total number of biopsies	51	26	25
Malignant and premalignant	22	11	11
Invasive ductal carcinoma (IDC)	20	10	10
Invasive lobular carcinoma (ILC)	2	1	1
Benign	29	15	14
Adipose, fibroadipose	2	1	1
Fibroglandular, fibrous, glandular	21	11	10
Fibroadenoma, papilloma	6	3	3